The current issue and full text archive of this journal is available on Emerald Insight at:
https://www.emerald.com/insight/0961-5539.htm

Received 11 October 2020
Revised 15 January 2021
Accepted 21 January 2021

On heat transfer and flow characteristics of jets impinging onto concave surface with varying bleeding arrangements

Dandan Qiu
Harbin Institute of Technology, Harbin, China

Lei Luo
School of Energy Science and Engineering, Harbin Institute of Technology, Harbin, China

Zhiqi Zhao and Songtao Wang
Harbin Institute of Technology, Harbin, China

Zhongqi Wang
School of Energy Science and Engineering, Harbin Institute of Technology, Harbin, China, and

Bengt Ake Sunden
Department of Energy Sciences, Lund University, Lund, Sweden

Abstract

Purpose – The purpose of this study is to investigate the effects of film holes' arrangements and jet Reynolds number on flow structure and heat transfer characteristics of jet impingement conjugated with film cooling in a semicylinder double wall channel.

Design/methodology/approach – Numerical simulations are used in this research. Streamlines on different sections, skin-friction lines, velocity, wall shear stress and turbulent kinetic energy contours near the concave target wall and vortices in the double channel are presented. Local Nusselt number contours and surface averaged Nusselt numbers are also obtained. Topology analysis is applied to further understand the fluid flow and is used in analyzing the heat transfer characteristics.

© Dandan Qiu, Lei Luo, Zhiqi Zhao, Songtao Wang, Zhongqi Wang and Bengt Ake Sunden. Published by Emerald Publishing Limited. This article is published under the Creative Commons Attribution (CC BY 4.0) licence. Anyone may reproduce, distribute, translate and create derivative works of this article (for both commercial and non-commercial purposes), subject to full attribution to the original publication and authors. The full terms of this licence may be seen at http://creativecommons.org/licences/by/4.0/legalcode

This work was supported by the National Natural Science Foundation of China [grant number 51706051]; China Postdoctoral Science Foundation funded project [grant number 2017M620116]; and China Postdoctoral Science Foundation funded project [grant number 2017M621268]. The simulations were performed on resources provided by the Swedish National Infrastructure for Computing (SNIC) at LUNARC and partially funded by the Swedish Research Council.

Conflict of interest: None declared.

International Journal of Numerical Methods for Heat & Fluid Flow
Vol. 15 No. 4, 2021
pp. 3642-3660
Emerald Publishing Limited
0961-5539
DOI 10.1108/HFF-10-2020-0630

Downloaded from ftp.nowpublishers.com/hff/article-pdf/31/12/3642/630499/hff-10-2020-0630.pdf by guest on 17 October 2026

Findings – It is found that the arrangement of side films positioned far from the center jets helps to enhance the flow disturbance and heat transfer behind the film holes. The heat transfer uniformity for the case of 55° films arrangement angle is most improved and the thermal performance is the highest in this study.

Originality/value – The film holes' arrangements effects on fluid flow and heat transfer in an impingement cooled concave channel are conducted. The flow structures in the channel and flow characteristics near target by topology pictures are first obtained for the confined film cooled impingement cases. The heat transfer distributions are analyzed with the flow characteristics. The highest heat transfer uniformity and thermal performance situation is obtained in present work.

Keywords Heat transfer, Film cooling, Jet impingement, Flow structure, Topology analysis

Paper type Research paper

Nomenclature

d_f = film diameter [mm];
d_j = jet diameter [mm];
D = target wall diameter [mm];
h = Heat transfer coefficient [W/(m^2.K)];
M = Mass flow rate at inlet [kg/s];
Nu = Nusselt number [−];
Nu_{ave} = Area-averaged Nusselt number [−];
$Nu_{ave,b}$ = Area-averaged Nusselt number for baseline [−];
P = Jet-to-jet/film-to-film distance for the same line jets/film holes at Y direction [mm];
P_i = Inlet mass flow average pressure [Pa];
P_o = Outlet mass flow average pressure [Pa];
q = Heat flux [W/m^2];
Re = Jet Reynolds number [−];
S = Stream-wise along the concave target surface [−];
TKE = Relative turbulence kinetic energy, nondimensionalized by u_i^2 [−];
T_i = Jet inlet temperature [K];
T_w = Impingement wall temperature [K];
u_i = Jet inlet velocity [m/s];
Z = Jet-to-target distance [mm];
θ = Degree between the middle array jets and side film arrays [°];
λ = Fluid thermal conductivity [W/(m.K)];
μ = Fluid dynamic viscosity [Pa.s];
ρ = Fluid density [kg/m^3]; and
τ_w = Wall shear stress [Pa].

1. Introduction

Due to its high potential in enhancing local heat transfer, jet impingement has been widely used in turbine thermal load components, especially for the highest heat load portion – the blade leading edge, which directly suffers hot gas from combustor (Kwak and Han, 2002).

Many significant works spent much efforts on the effects of jet Reynolds number, jet nozzle configuration, jet-to-target spacing, target arrangement and jet inclination angle on single jet impinging onto a confined or an unconfined concave or convex surface (Yang *et al.*, 1999; Rahman *et al.*, 2010; Qiu *et al.*, 2019; Cornaro *et al.*, 1999; Luo *et al.*, 2016; Lee *et al.*, 2007; Yang and Hwang, 2004).

In real applications, multiple impingement jets are commonly used. Concerning the parameters mentioned above, the jet arrangement plays an important role of a single row or

Downloaded from ftp.nowpublishers.com/hff/article-pdf/31/12/3642/630499/hff-10-2020-0630.pdf by guest on 17 October 2026

arrays of jets situations. Concerning the single case, the jets are often arranged at the center of the surface. Chupp *et al.* (1969) performed an experiment to investigate how the heat transfer is influenced by jet Reynolds number, jet-to-target/jet-to-jet spacing and target curvature for an array of round jets impinging onto a confined concave surface. They presented dimensionless correlations of the area-averaged and stagnation point Nusselt numbers. Metzger *et al.* (1969) experimentally summarized the correlations of maximum and local Stanton number of a confined concave channel. Efforts on effects of jet Reynolds number, jet-to-target/jet-to-jet spacing and target curvature on local Nusselt number distributions of a single array of jets impinging onto a confined or an unconfined concave surface were conducted experimentally (Bunker and Metzger, 1990; Patil and Vedula, 2018) and numerically (Kumar and Prasad, 2008). Yang *et al.* (2014) numerically conducted unsteady predictions of flow characteristics in a cylinder channel with a single row impingement jets at a constant jet Reynolds number 15,000. For arrays of jet arrangements, the Nusselt number distributions of two staggered arrays of impingement jets on a confined concave channel with changing jet Reynolds number were experimentally investigated with the transient liquid crystal technique by Calzada and Alvarez (2012). Jung *et al.* (2018) performed an investigation numerically and experimentally about the influence of injection angle on fluid flow and heat transfer for three staggered arrays of impingement jets. More recently, Qiu *et al.* (2020) predicted the vortical structure of jets impinging onto a confined curved surface for three arrays of jets arranged inline and staggered and further analyzed the local heat transfer characteristics with the fluid flow identified by numerical simulations.

At the blade leading edge of a high-pressure turbine blade, impingement is often applied conjugated with film cooling. Metzger and Bunker (1990) designed an experiment to measure the local heat transfer characteristics of blade impingement-cooled leading edge with bleedings and found that the change of the jet-to-film position can cause significant variations of the leading-edge temperature. Taslim *et al.* (2003) performed a study to compare the effects of the target wall roughening conditions on an impingement-cooled blade leading edge with film holes numerically and experimentally. They claimed that the numerical works presented good agreement with the experimental results. It was found that impingement on the smooth target produced the highest overall heat transfer coefficients followed by the notched-horseshoe ribs and horseshoe geometries. Taslim and Khanicheh (2006) conducted numerical and experimental works on the influence of varying film extraction patterns on the heat transfer coefficients of an airfoil leading edge with impingement cooling. The results inferred that the presence of film holes along the leading edge enhanced the internal impingement heat transfer coefficients significantly compared with the case without film holes. Yang *et al.* (2013) measured the heat transfer coefficient on a 2/3 cylinder leading edge model with impingement cooling and varying film cooling arrangements by the transient liquid crystal technique and compared with numerical simulation works. The results recommended the hole position for the best cooling performance. Andrei *et al.* (2013) evaluated the heat transfer coefficients on a real-engine leading edge cooling system characterized by racetrack-shaped crossover holes, showerhead and film cooling extraction holes and large fins both experimentally and numerically. They highlighted that asymmetric mass flow extraction and variable crossflow conditions slightly influence the Nusselt number. Wang *et al.* (2018) investigated the effect of jet impinging position on the heat transfer of a leading edge with extractions and showed that the tangential jet provided more uniform heat transfer distribution than the normal jet with similar area averaged Nusselt numbers. Luo *et al.* (2020) presented a numerical analysis of the pin-fins' arrangement in a Lamilloy cooling system. The results showed the optimum

Downloaded from ftp.nowpublishers.com/hff/article-pdf/31/12/3642/630499/hff-10-2020-0630.pdf by guest on 17 October 2026

location and diameter of pin-fin with high heat transfer enhancement and relatively low pressure loss.

Impingement-cooled blade leading edge with extractions has been extensively investigated but mainly with the flow and geometry effects on the local or averaged heat transfer coefficient. Very limited published work indicates the relationship between flow structure and heat transfer characteristics of impinging-cooled leading edge conjugated with varying film arrangement. In this study, the relationship between flow structure and heat transfer characteristics of a single array of jets impingement conjugated with two staggered arrays of film holes of a semicylinder double wall channel are numerically investigated. The effects of film hole arrangements and jet Reynolds number (10,000–40,000) on the fluid flow and heat transfer are also presented. The characteristics of the flow structure (vortices, streamlines and skin-friction lines) and heat transfer (local Nusselt number contours and surface averaged Nusselt numbers) for different cases are obtained. Topology analysis is also applied to understand the fluid flow which is then applied to analyze the local heat transfer characteristics.

2. Problem description

2.1 Physical model

According to the previous discussions, jet impingement conjugated with film cooling is usually applied at the blade leading edge due to its high heat transfer enhancement. As shown in Figure 1(a), the blade leading edge cooling structure is simplified to a semicylinder double wall channel with a center array of jets and two side arrays of film cooling holes. The degree θ between the center jets and side films is changing from 0° to 55° [Figure 1(a)]. The case of $\theta = 0°$ is set as the baseline, in which only one array of film holes is arranged. From the top view [Figure 1(b)], the side arrays of film holes (black circles) are staggered in relation to the center array of jets (shadow circles) with jet-to-jet/film-to-film spacing P/d_j = 4. All parameters presented are normalized by the jet diameter d_j. The whole area of film cooling holes is constant for all cases and the film hole diameter for the baseline d_f is equal to the jet diameter d_j. The jet-to-target distance Z/d_j and relative surface curvature D/d_j are 1 and 10, respectively. The detailed information of the cases is shown in Table 1. The jet Reynolds number varies from 10,000 to 40,000 (Patil and Vedula, 2018).

2.2 Boundary conditions

This study reveals the effects of jet Reynolds number *Re* and film holes arrangement on fluid flow and heat transfer characteristics of a semicylinder double wall jet impingement cooling system conjugated with film cooling. As presented in Figure 1, the target wall is set as no-slip and an isothermal wall condition. No-slip and adiabatic wall boundary condition are applied to the other surfaces. A mass flow rate at the inlet and isothermal boundary condition with 5% turbulence intensity are used at the jet inlet. A pressure outlet boundary is set at the film hole outlet. The temperature difference between the jet inlet and target wall is 41 K. The fluid is considered as an ideal gas.

2.3 Topology of skin-friction fields

Topology analysis is a method to understand the three-dimensional separated flows. It uses skin-friction lines coupled with the critical point theory (Legendre, 1956; Poincaré, 1882; Hirschel *et al.*, 2014) and has been applied in some research and engineering works (Gbadebo *et al.*, 2005; Zhao *et al.*, 2020; Kan *et al.*, 2016).

Downloaded from ftp.nowpublishers.com/hff/article-pdf/31/12/3642/630499/hff-10-2020-0630.pdf by guest on 17 October 2026

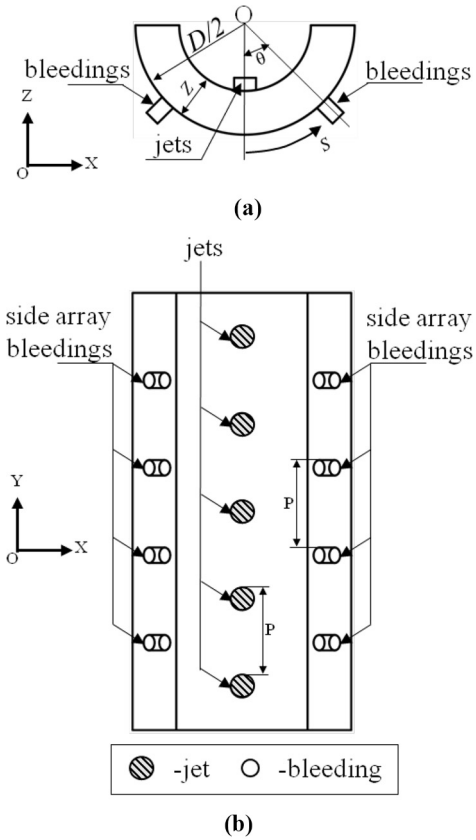

Figure 1.
Schematic picture of the fluid flow model

Table 1.
Detailed information of the cases

Cases	Film arrangement	P/d_j	θ (°)	d_f/d_j
Baseline	1 row/same line	4	–	1
Case 1	2 rows/staggered	4	15	0.707
Case 2	2 rows/staggered	4	25	0.707
Case 3	2 rows/staggered	4	35	0.707
Case 4	2 rows/staggered	4	45	0.707
Case 5	2 rows/staggered	4	55	0.707

Four main critical points(spiral node, attachment node, separation node and saddle) and two lines (attachment line and separation line) are used in the present work. The detailed definitions are presented in Figure 2 (Délery, 2001).

3. Computational solution method

Three-dimensional, nonrotating, steady and compressible simulations have been performed with the commercial software FLUENT (2018). The second-order accuracy option and phase

Downloaded from ftp.nowpublishers.com/hff/article-pdf/31/12/3642/630499/hff-10-2020-0630.pdf by guest on 17 October 2026

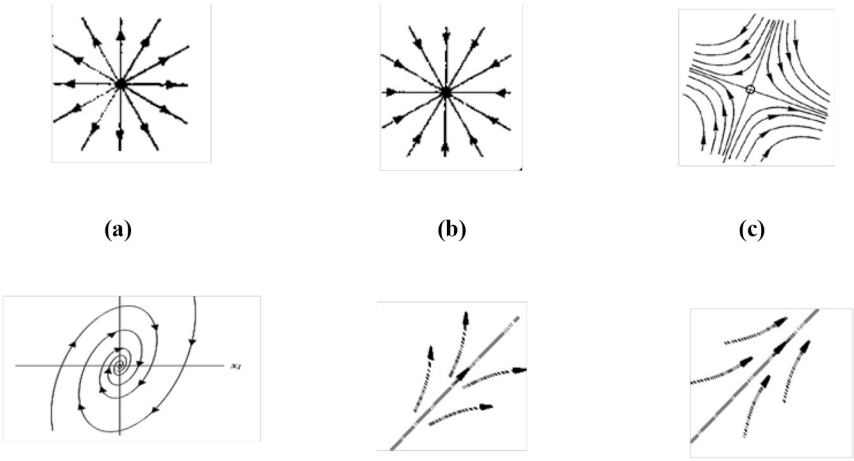

Notes: (a) Attachment node; (b) separation node; (c) saddle; (d) spiral node; (e) attachment line; (f) sepration line

Figure 2. (a-d) Different critical points, (e) attachment line and (f) separation line (Délery, 2001)

coupled semi implict pressure linked equations algorithm are applied. The computation is regarded to be converged as the residuals below 1×10^{-5} for the continuity equation, velocity, turbulence and energy equations.

3.1 Governing equations

The steady viscous fluid flow motion is governed by the following equations (Versteeg and Malalasekera, 2007):

Continuity equation:

$$\frac{\partial(\rho \overline{u}_i)}{\partial x_i} = 0 \tag{1}$$

Momentum equation:

$$\frac{\partial(\ \rho \overline{u}_i \overline{u}_j)}{\partial x_j} = -\frac{\partial \overline{P}}{\partial x_i} + \frac{\partial}{\partial x_j}\left((\mu + \mu_t)\left(\frac{\partial \overline{u}_i}{\partial x_j} + \frac{\partial \overline{u}_j}{\partial x_i}\right)\right) \tag{2}$$

Energy equation for fluid:

$$C_p \overline{u}_i \frac{\partial \rho \overline{T}}{\partial x_i} = \frac{\partial}{\partial x_i}\left(\lambda \frac{\partial \overline{T}}{\partial x_i}\right) - C_p \frac{\partial}{\partial x_i}\left(\frac{\mu_t}{Pr_t}\frac{\partial \overline{T}}{\partial x_i}\right) \tag{3}$$

The computations were conducted by using a Reynolds-averaged Navier–Stokes model combined with the kω-baseline turbulence model (BSL). The kω-BSL is believed to improve the predictive capability for complex turbulent flows with flow swirling and separation and

Downloaded from ftp.nowpublishers.com/hff/article-pdf/31/12/3642/630499/hff-10-2020-0630.pdf by guest on 17 October 2026

it is also claimed to offer the best trade-off between accuracy and computational cost for the parameters considered (Versteeg and Malalasekera, 2007; Menter, 1994; Wallin and Johansson, 2000). Therefore, the kω-BSL turbulence model is used and the following equations are applied.

The equation of the turbulent kinetic energy k reads as follows:

$$\frac{\partial(\rho k)}{\partial t}+\frac{\partial}{\partial x_i}(\rho k u_i)=\frac{\partial}{\partial x_i}\left[\left(\mu+\frac{\mu_t}{\sigma_{k3}}\right)\frac{\partial k}{\partial x_i}\right]+P_k-\beta^*\rho\omega k \tag{4}$$

The equation of the dissipation rate ω reads as follows:

$$\begin{aligned}\frac{\partial(\rho\omega)}{\partial t}+\frac{\partial}{\partial x_i}(\rho\omega u_i)=&\frac{\partial}{\partial x_i}\left[\left(\mu+\frac{\mu_t}{\sigma_{\omega 3}}\right)\frac{\partial\omega}{\partial x_i}\right]\\&+(1-F_1)\frac{2\rho}{\sigma_{\omega 2}\omega}\frac{\partial k}{\partial x_i}\frac{\partial\omega}{\partial x_i}+\alpha_3\frac{\omega}{k}P_k-\beta_3\rho\omega^2\end{aligned} \tag{5}$$

where

$$\sigma_{k3}=F_1\sigma_{k1}+(1-F_1)\sigma_{k2} \tag{6}$$

$$\sigma_{\omega 3}=F_1\sigma_{\omega 1}+(1-F_1)\sigma_{\omega 2} \tag{7}$$

$$\beta_3=F_1\beta_1+(1-F_1)\beta_2 \tag{8}$$

$$\alpha_3=F_1\alpha_1+(1-F_1)\alpha_2 \tag{9}$$

$$\mu_t=\rho\frac{k}{\omega} \tag{10}$$

$$P_k=\mu_t\left(\frac{\partial u_i}{\partial x_j}+\frac{\partial u_j}{\partial x_i}\right)\frac{\partial u_i}{\partial x_j}-\frac{2}{3}\frac{\partial u_k}{\partial x_k}\left(3\mu_t\frac{\partial u_k}{\partial x_k}+\rho k\right) \tag{11}$$

$$F_1=\tanh\left(arg_1^4\right) \tag{12}$$

$$arg_1=\min\left[\max\left(\frac{\sqrt{k}}{\beta^*\omega d},\frac{500v}{d^2\omega}\right),\frac{4\rho\sigma_{\omega 2}k}{CD_{k\omega}d^2}\right. \tag{13}$$

$$\mathrm{CD}_{\mathrm{k}\omega}=\max\left(2\ \rho\sigma_{\ \omega 2}\frac{1}{\omega}\frac{\partial \mathrm{k}}{\partial \mathrm{x_i}}\frac{\partial \mathrm{w}}{\partial \mathrm{x_i}},10^{-20}\right) \tag{14}$$

The constants have the values $\sigma_{k1}=2$, $\sigma_{k2}=1$, $\sigma_{\omega 1}=2$, $\sigma_{\omega 2}=1/0.856$, $\beta_1=0.075$, $\beta_2=0.0828$, $\beta^*=0.09$, $\alpha_1=5/9$, $\alpha_2=0.44$, $A_1=1.245$, $A_2=0$, $A_3=1.8$, $A_4=2.25$, $C_\mu=0.09$.

Downloaded from ftp.nowpublishers.com/hff/article-pdf/31/12/3642/630499/hff-10-2020-0630.pdf by guest on 17 October 2026

3.2 Mesh information

As shown in Figure 3, a structured mesh is generated by the ICEM computational fluid dynamics (CFD) (2018) with quality above 0.6. Near-wall meshes with y+ $\sim$ 1 are applied. Grid independence validation has been performed for the baseline to make certain that the simulations are reasonable accurate with low computational efforts. As presented in Figure 4, the laterally averaged Nusselt number on the target wall and pressure along the stream-wise direction for changing mesh numbers are provided. It is found that there are no significant differences between the meshes 6.5 and 12 million. To save the computational demands, the grid configurations with 6.5 million cells are applied in this work.

3.3 Data reduction

The Reynolds number is defined as:

$$Re = \frac{\rho u_i d_j}{\mu} \tag{15}$$

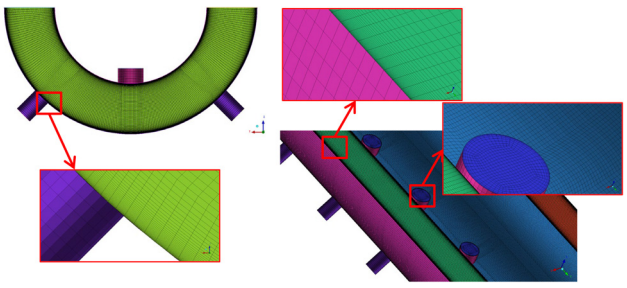

Figure 3.
Grid of Case 4

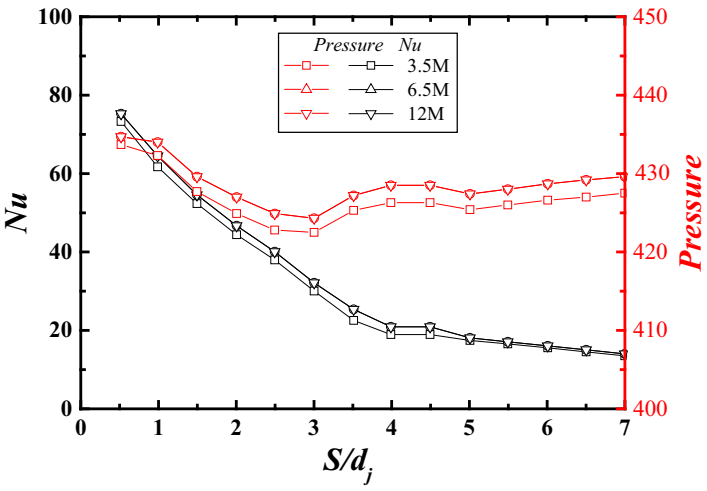

Figure 4.
Mesh independence study (baseline)

Downloaded from ftp.nowpublishers.com/hff/article-pdf/31/12/3642/630499/hff-10-2020-0630.pdf by guest on 17 October 2026

The heat transfer coefficient h is defined as:

$$h = \frac{q}{T_i - T_w} \tag{16}$$

The Nusselt number is defined as:

$$Nu = h \times \frac{d_j}{\lambda} \tag{17}$$

The pumping power (Bergman *et al.*, 2011) is defined as:

$$P = (P_i - P_o) * M/\rho \tag{18}$$

where u_i is the mean velocity at the jet inlet, d_j is the hydraulic diameter of the jet and ρ and μ are the fluid density and dynamic viscosity, respectively. q is the heat flux, λ is the fluid thermal conductivity, T_i and T_w are the temperature of the jet inlet and target wall, respectively. P_i and P_o are the mass flow average total pressures at the jet inlet and outlet, respectively. M is mass flow rate at the inlet.

3.4 CFD validation

In this work, the laterally local Nusselt number and averaged Nusselt number are compared with the experimental data by Patil and Vedula (2018) to verify the accuracy of the computations. The case with D/d_j = 10, P/d_j = 4, Z/d_j = 2, Re = 50,000 is considered for comparison. As presented in Figure 5, the numerical validations are conducted by comparing the laterally variations for some turbulence models in FLUENT with the experimental data by Patil and Vedula (2018). The error bar of the experimental data is set as 10% which is the maximum uncertainty of the experiment. It is obvious that the trends of the kω-BSL model are very similar with the experiments and the maximum inaccuracy is satisfactory. Concerning the average parameters, the average Nusselt numbers are presented in Table 2. The maximum difference between the numerical and experimental

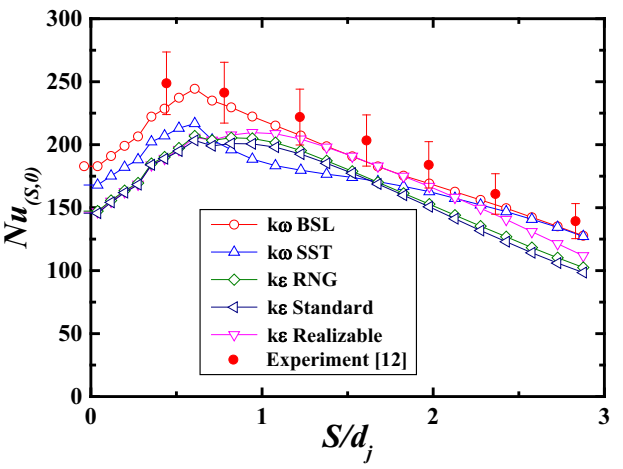

Figure 5. Comparison line of Y/d_j = 0 Nusselt number distributions in stream wise. The error bar is 10%. The experimental data is from the work of Patil and Vedula (2018)

Downloaded from ftp.nowpublishers.com/hff/article-pdf/31/12/3642/630499/hff-10-2020-0630.pdf by guest on 17 October 2026

data is 5.4% which is lower than the experimental uncertainty, i.e. 10%. Therefore, the kω-BSL turbulence model is considered acceptable in this work.

4. Results and discussions

4.1 Fluid flow characteristics

The overall heat transfer performance is highly related to the local heat transfer characteristics which are significantly affected by the fluid flow. To understand the effect of the conjugated film holes' arrangement on fluid flow characteristics for jets impinging onto a confined concave surface, streamlines at different sections, skin-friction lines near the target wall, topology pictures and vortices in the channel of the baseline and Case 5 are introduced. Due to the symmetry characteristics of the geometry and fluid flow, half part ($X/d_j > 0$) is presented for the near-wall surface skin-friction lines, vortex figures and Nusselt number plots. To reveal the similarity of the fluid characteristics, figures of the vortices around the middle jet are presented.

Figure 6 provides the vortices with the λ^2-(a-b) criterion, streamlines at (c) different sections of the baseline. Due to the symmetry of the flow and to avoid confusion, only the

Table 2. Different included angle averaged Nusselt number comparison between kω-BSL turbulence model results and experimental work

	Nu_{ave} ($\theta = -25° - 25°$)	Nu_{ave} ($\theta = -45° - 45°$)
Experiment [12]	205.68	160.67
Present	200.26	151.93
Difference	2.6%	5.4%

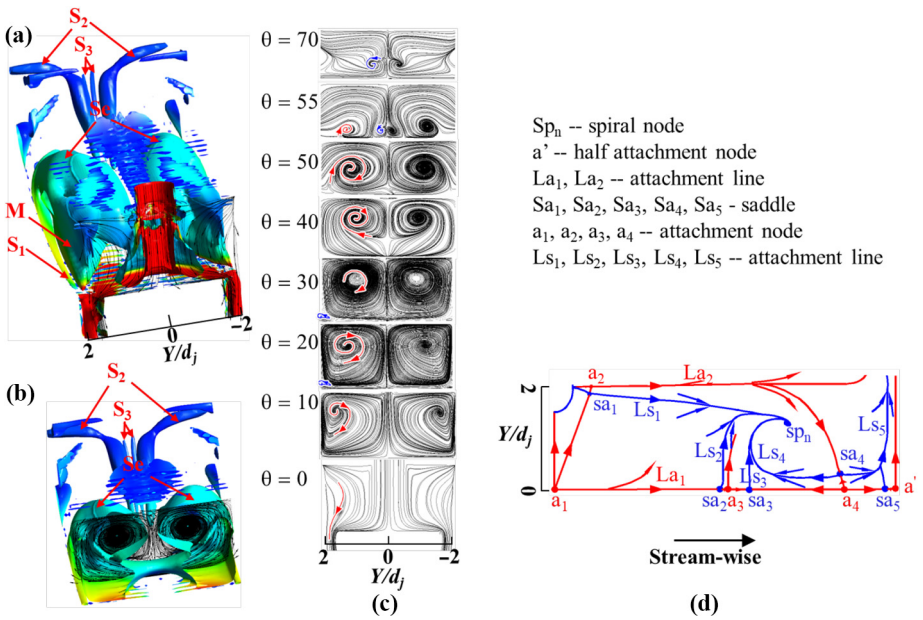

Figure 6. Fluid flow of middle jet for baseline at $Re = 20{,}000$: (a-b) vortices colored with velocity (M – primary vortices; Se – separation vortices; S_1, S_2, S_3 – secondary vortices); (c) streamlines at different sections; (d) topology picture

Downloaded from ftp.nowpublishers.com/hff/article-pdf/31/12/3642/630499/hff-10-2020-0630.pdf by guest on 17 October 2026

system of $2 \geq Y/d_j \geq 0$ is discussed. As shown in Figure 6(a), the main vortex (marked as M) can be observed, which coincides with an outward clockwise circulation of the streamlines [θ from 0° to 30° in Figure 6(c)]. This unsteady flow can be attributed to the interactions of adjacent jets and the suction effect of the film hole. Below the main vortex M, a secondary vortex S_1 [Figure 6(a)] and inward anticlockwise rotation [θ = 20°, 30° in Figure 6(c)] are found near $Y/d_j = 2$, which can be related to the restriction effect of the up-wash main flow (main vortex M) and target wall. Other secondary flows, marked as S_2, S_3 [Figure 6(a, b)] and parallel recirculation [θ = 55°, 70° in Figure 5(c)] are also found near $Y/d_j = 0$. A steady separated flow occurs which can be observed in the pictures of the vortices as the vortex Se marked in Figure 6(b) and the internal clockwise circulations shown in Figure 6(c) (θ = 55°, 50°, 40°). Concerning the topology picture [Figure 6(d)], the attachment node a_1 can be related to the jet impinging. With the interaction of the main flow (clockwise vortex M) and secondary flow (counterclockwise vortex S_1), the separation line Ls_1 is formed. The appearance of the attachment lines La_1 and La_2 can be attributed to the interactions of adjacent vortices M around $Y/d_j = 0$ and S_1 around $Y/d_j = 2$, respectively. Along the stream-wise direction, the position of the spiral node Sp_n coincides with the appearance of the separation vortex Se which is spiraled by the separation lines Ls_1 (from saddle sa_1), Ls_2 (from saddle sa_2), Ls_3 (from saddle sa_3) and Ls_4 (from saddle sa_4). The separation line Ls_5 shows similar trends with the secondary vortex S_1. The region between separation line Ls_4 and center red attachment line ($Y/d_j = 0$) coincides with the secondary vortex S_3. Between the separation lines Ls_2 and Ls_3, another secondary flow region might be detected by the topology analysis.

As film holes positioned farther from the center array jets, the flow characteristics change. Figure 7 presents pictures of vortices with λ^2-(a-b) criterion, streamlines at (c) different sections of Case 5. Compared with the baseline, a similar main vortex M and secondary vortex S_{12} with paralleling unsteady outward clockwise circulation in streamlines [θ = 0° –25°, Figure 7(c)] and inward anticlockwise circulation around $Y/d_j = 2$ [θ = 0°–45° in Figure 7(c)] also occur. The corresponding attachment lines La_1, La_2 and the separation line Ls_1 due to the interaction of adjacent main vortices M, between main vortex M and secondary vortex S_1 and neighboring secondary vortices S_1 are clearly shown in Figure 7(d). The most different styles are the appearance of secondary vortex S_4, vortex S and the absence of the separation vortex Se and secondary vortices S_2, S_3. The vortex S_4 around $Y/d_j = 0$ is related to the interaction between vortex M and the upper wall. The corresponding circulation in the streamlines is observed [θ = 15° – 40°, Figure 7(c)]. The L type vortex S moves against the stream-wise direction and toward the $Y/d_j = 0$ section [Figure 7(c), from θ = 70° – 40°] which might be attributed to the film suction effect.

4.2 Local heat transfer characteristics

On the basis of the discussion, the local wall heat transfer characteristics are analyzed with the wall skin-friction lines, topology pictures, wall dimensionless velocity, wall shear stress and turbulence kinetic energy (*TKE*) contours. The quarter plots of wall distributions are provided in Figures 8 and 9 for the baseline and Case 5, respectively, due to the symmetry of geometry and fluid flow. Generally, the Nusselt number distributions show higher values around the attachment lines [red lines presented in Figures 8(a) and 9(a)]. As the flow attaches to the target wall, the velocity, wall shear stress and *TKE* present high levels. In contrast, the values near the separation lines [blue lines presented in Figures 8(a) and 9(a)] present low levels.

For the baseline, it is obvious that relative high velocity, wall shear stress and turbulence kinetic energy values occur around the impingement region (marked as A) and then

Downloaded from ftp.nowpublishers.com/hff/article-pdf/31/12/3642/630499/hff-10-2020-0630.pdf by guest on 17 October 2026

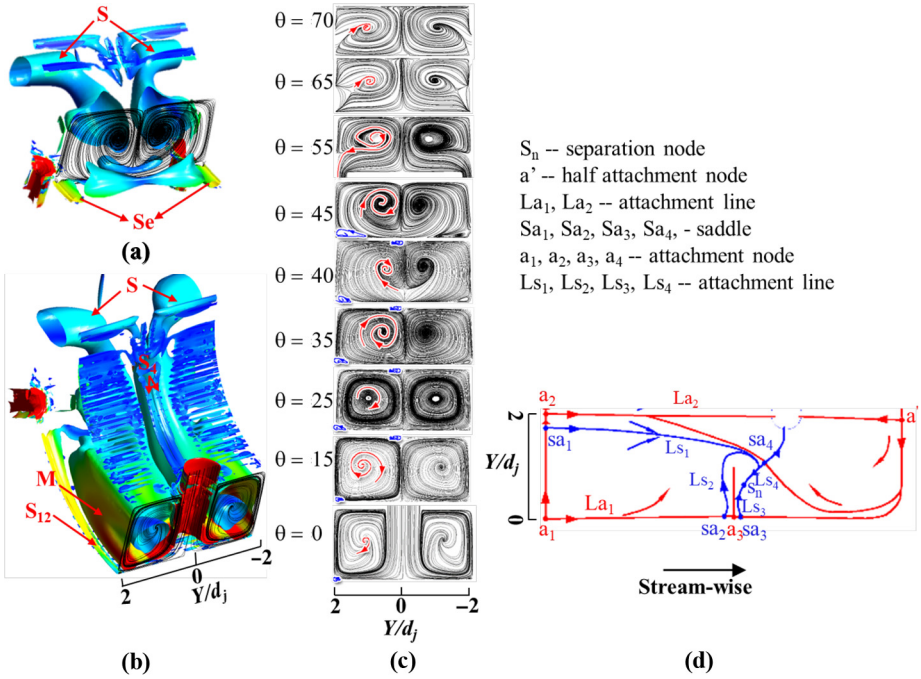

Figure 7. Fluid flow of middle jet for Case 5 at $Re = 20{,}000$: (a-b) vortices colored with velocity (M – primary vortices; S – L-type vortices; S_1, S_4 – secondary vortices); (c) streamlines at different sections; (d) topology picture

decrease along the stream-wise direction [Figures 8(c-e)]. This can be attributed to the main flow impinging effect of jets which can be the reason of the significantly enhanced heat transfer region A marked in Nusselt number contours [Figure 8(b)]. Along the stream-wise direction, a low value region (marked as B) coincides with the region enclosed by some separation lines [Figure 8(a)], which can be related to the secondary flow mentioned above. Around the spiral node, the values of the Nusselt number, velocity, wall shear stress and *TKE* are also very low. This can be attributed to the movement of separation vortices. As the flow separates from the target wall and generates the separation vortices Se with low velocity, wall shear stress and *TKE* distributions, which may lead to a thinner flow boundary layer and thus result in a low heat transfer enhancement. Further away from the center jet positions, the values are also very low near the end of the target wall in the stream-wise direction. This can be related to the low energy secondary vortices S_2 discussed in Figure 6. Between the center jets, the heat transfer near the film holes is significantly enhanced and the flow parameters also show high values, which can be related to the suction effect. In Figure 8, another high value region marked as C can be observed around the attachment lines of Y/d_j = 2, 6, 10. This appearance of region C coincides with the secondary vortex S_1.

Comparing the topology pictures of Case 5 and the baseline, the disappearance of vortex Se, S_2, S_3 can also be clearly observed. Concerning the flow characteristics and heat transfer distributions (Figure 9), high values of region A and around the film holes, low values (region B) at the recircled separation lines and relative high values (region C) around the attachment line La2 are also observed. Not like the baseline, at the backward of the film holes, the Nusselt number contours present higher levels coinciding with a relative high

Downloaded from ftp.nowpublishers.com/hff/article-pdf/31/12/3642/630499/hff-10-2020-0630.pdf by guest on 17 October 2026

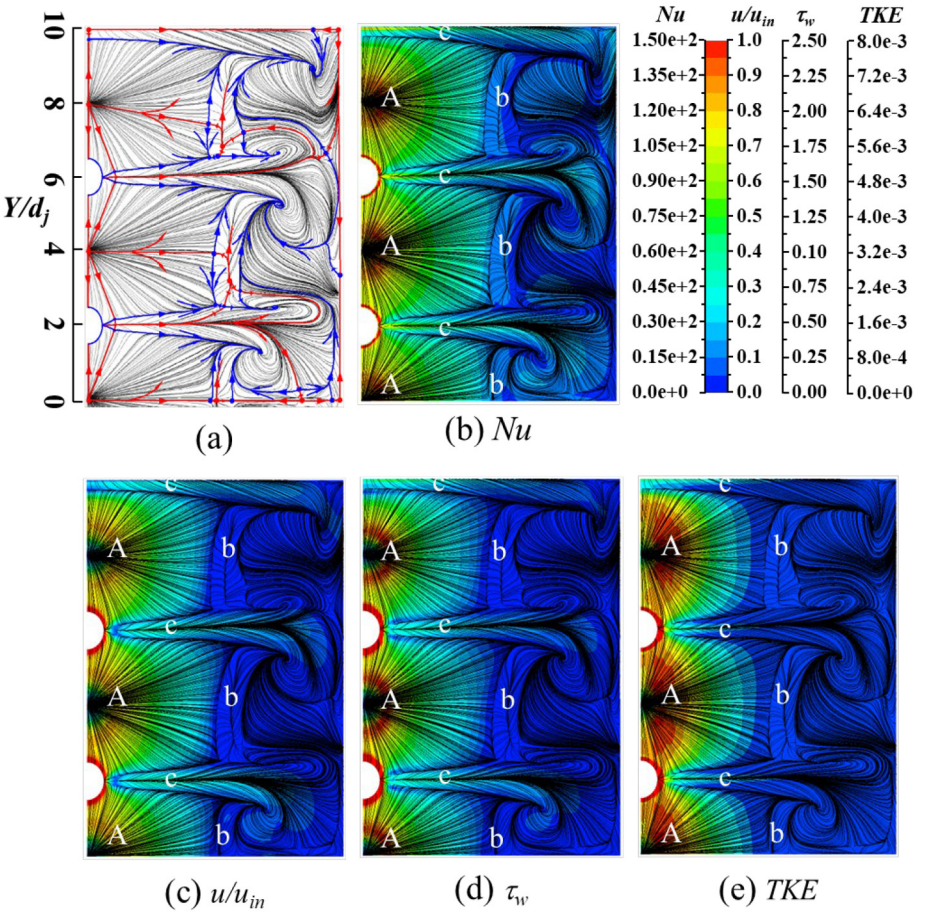

Figure 8.
(a) Skin-friction lines with topology picture, (b) Nusselt number, (c) dimensionless velocity, (d) wall shear stress and relative turbulence kinetic energy (*TKE*) near target wall of baseline. Red line-attachment line; blue line-separation line

level in the distributions of the dimensionless velocity and wall shear stress. The flow disturbance behind the holes is stronger. This can be related to the appearance of vortex S which may be attributed to the strong suction effect of the film holes.

4.3 Overall discussion

Figure 10 provides the relative area averaged Nusselt numbers for different cases and different Surfaces 1–3 at $Re = 20{,}000$. Surface 1 is set as the region of $\theta = -25°$ to 25°; Surface 2 is defined the region of $\theta = -45°$ to 45°; and $\theta = -90°$ to 90° is for the region of Surface 3. $Nu_{ave,b}$ is the averaged Nusselt number of the baseline. The detailed surface Nusselt number distributions with skin-friction lines of quarter part are provided in Figure 11. Surface 1 is circled by a red rectangle and the blue one is for Surface 2.

As presented in Figure 10, $Nu_{ave}/Nu_{ave,b}$ for Surface 1 shows an increase as the film arrays are positioned at $\theta = 15°$, whereas a decrease appears from $\theta = 15°$–35° and finally a relative constant level is found up to $\theta = 55°$. By comparing baseline and Case 1, it is observed that the high values of region A and the film region are roughly the same. The

Downloaded from ftp.nowpublishers.com/hff/article-pdf/31/12/3642/630499/hff-10-2020-0630.pdf by guest on 17 October 2026

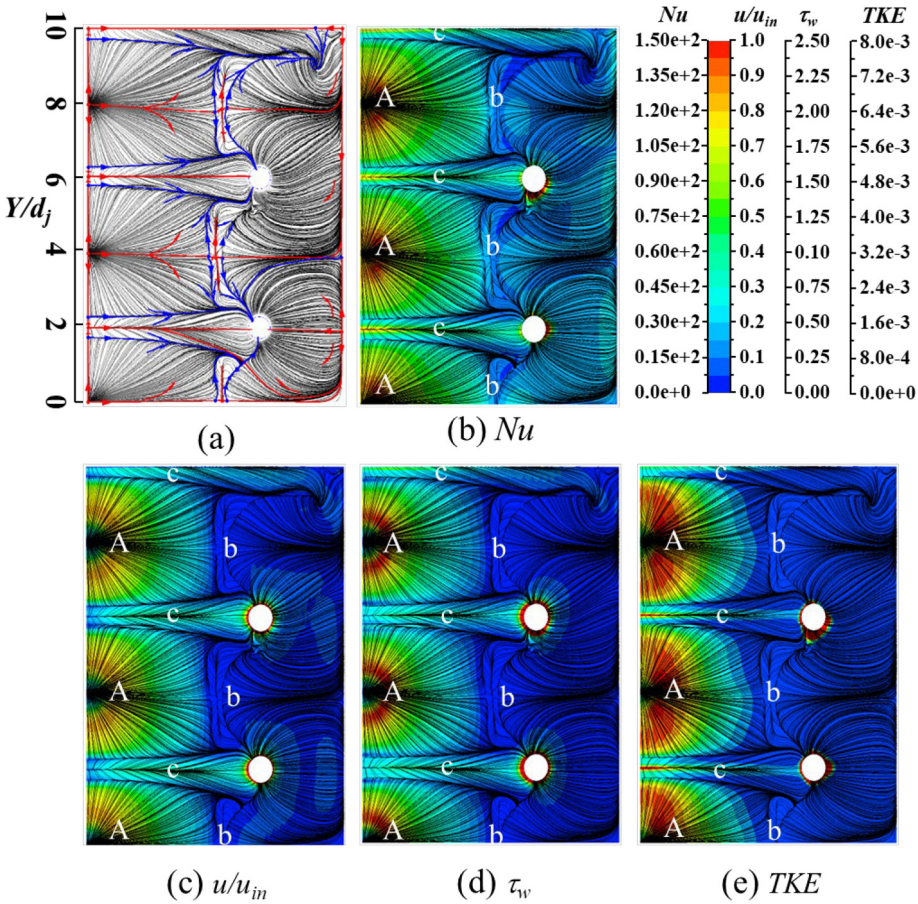

Figure 9. (a) Skin-friction lines with topology picture, (b) Nusselt number, (c) dimensionless velocity, (d) wall shear stress and relative turbulence kinetic energy (*TKE*) near target wall of Case 5. Red line-attachment line; blue line-separation line

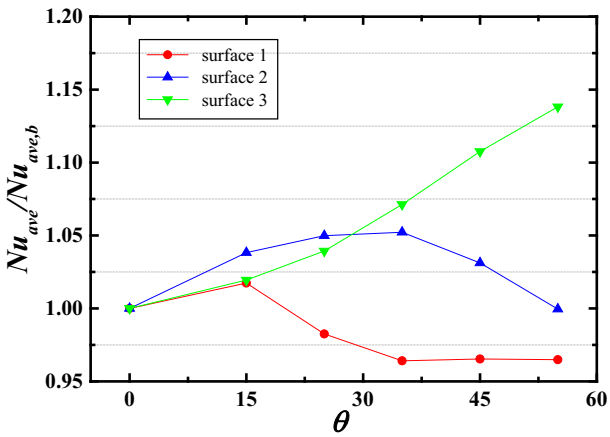

Figure 10. Relative area averaged Nusselt number averaged from Surfaces 1–3 at $Re = 20{,}000$. $Nu_{ave,b}$ is the number of baseline

Downloaded from ftp.nowpublishers.com/hff/article-pdf/31/12/3642/630499/hff-10-2020-0630.pdf by guest on 17 October 2026

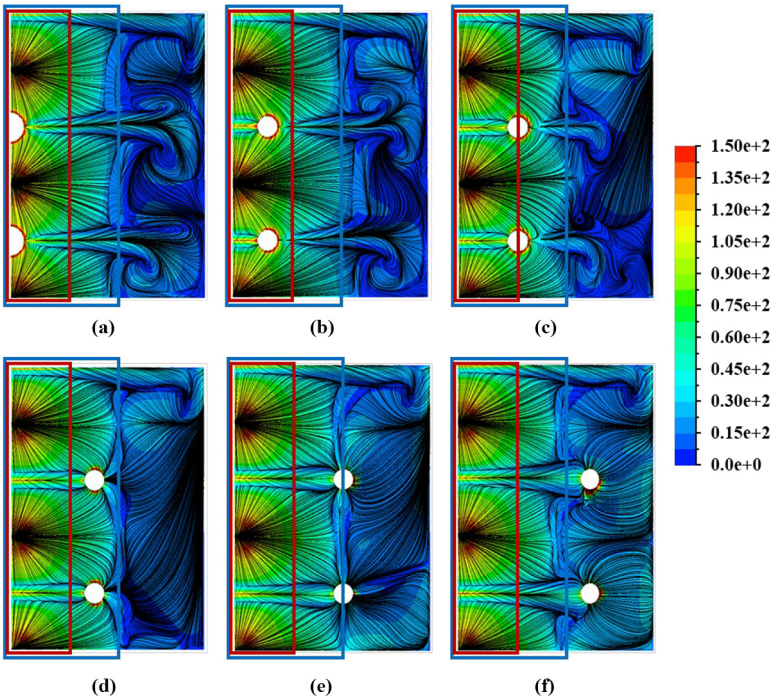

Notes: (a) Baseline; (b) $\theta = 15°$; (c) $\theta = 25°$; (d) $\theta = 35°$; (e) $\theta = 45°$; (f) $\theta = 55°$

Figure 11. Local Nusselt number distributions conjugated with skin-friction lines for different cases at $Re = 20{,}000$. Surface 1 is circled by red rectangle, Surface 2 is by blue rectangle

appearance of the relative high value region C might be due to the secondary vortex S_{12}. The following decrease as θ changes from 15° to 35° can be related to the absence of a high region around the film holes due to the suction effect. The constant value of $Nu_{ave}/Nu_{ave,b}$ for Cases 3–5 can be due to the relative similar distributions for Surface 1. Thus, it can be confirmed that the arrangement of side array film holes provides little influence on the heat transfer enhancement of Surface 1 as $\theta > 35°$. For Surface 2, the averaged values, $Nu_{ave}/Nu_{ave,b}$, increase from 1 to 1.05 as θ changes from 0° to 35°, then decrease to 0.999 as θ changes from 35° to 55°. As shown in Figure 10, this increasing trend can be attributed to the absence of a low heat transfer region coinciding with the low energy region C [marked in Figures 8(c-e) and 9(c-e)] and enlarging the relatively high Nusselt number region due to the secondary vortex S_{12}. The value is less than unity for Case 5. This can be related to the appearance of the low heat transfer region due to the low energy region C [marked in Figures 9(c-e)] and the absence of high Nusselt numbers around the film holes. Concerning the whole surface averaged parameter, as shown in Figure 10, $Nu_{ave}/Nu_{ave,b}$ increases with increasing θ. This can be related to the strong suction effect of the film holes on the flow behind the holes along the stream-wise direction. The farther the film holes are arranged from the center jets, the stronger is the flow disturbance generated behind the film holes' region, where the heat transfer is more enhanced (Figure 11). For a specific case, $Nu_{ave}/Nu_{ave,b}$ increases by enlarging the evaluated surface (Surface 1 to Surface 3) for Cases 3–5 (θ from 35° to 55°). It can be inferred that the far away side film holes play an effective part for the heat transfer uniformity.

Downloaded from ftp.nowpublishers.com/hff/article-pdf/31/12/3642/630499/hff-10-2020-0630.pdf by guest on 17 October 2026

Figure 12(a) illustrates the averaged Nusselt number for Surfaces 1–3 and the relative pressure with varying Reynolds number and film holes arrangement. Generally, *Re* plays an unquestionable positive role in enhancing the heat transfer for all arrangements. The effect of the film holes arrangement on the heat transfer enhancement is independent of the Reynolds number. In Figure 12(b), a comparison of the area-averaged heat transfer coefficients of the target wall subject to the pumping power is provided. As illustrated by the curves, the heat transfer coefficient is slightly increased with an increasing θ from 0° to 55° at a constant pumping power. It could be inferred that the far away arrangement of the side film holes to the center jets shows a positive influence in increasing the thermal performance in this work.

5. Conclusions

In this study, the effects of arrangement of film holes on fluid flow and heat transfer characteristics are provided for jet impingement system conjugated with film cooling in a semicylinder double wall channel by numerically simulations. The detailed flow structures, flow characteristics influence on the local heat transfer distributions for two typical cases are discussed. The results show that the far away staggered film holes arrangement plays a

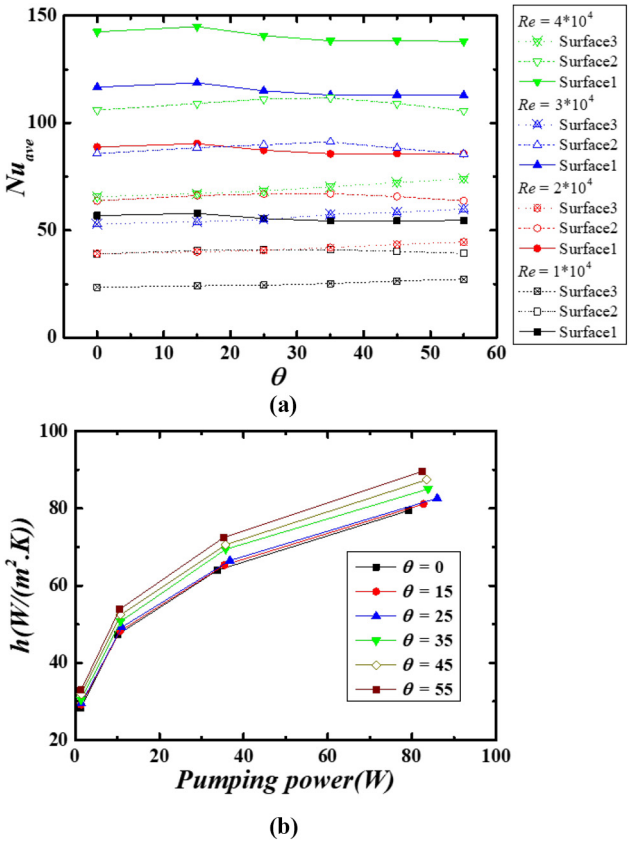

Figure 12.
(a) Area-averaged surface Nusselt number and thermal performance for varying cases and Reynolds number

Downloaded from ftp.nowpublishers.com/hff/article-pdf/31/12/3642/630499/hff-10-2020-0630.pdf by guest on 17 October 2026

positive role in heat transfer uniformity and thermal performance. The heat transfer uniformity and thermal performance are significantly improved for the cases of 35°–55° film holes' arrangement angle compared with the baseline due to the flow disturbance enhanced by the films suction effect. The case of 55° shows the most improved heat transfer uniformity and the thermal performance is the highest in this study.

References

Andrei, L., Carcasci, C., Da Soghe, R., Facchini, B., Maiuolo, F., Tarchi, L. and Zecchi, S. (2013), "Heat transfer measurements in a leading edge geometry with racetrack holes and film cooling extraction", *Journal of Turbomachinery*, Vol. 135 No. 3, p. 031020.

Bergman, T.L., Incropera, F.P., DeWitt, D.P. and Lavine, A.S. (2011), *Fundamentals of Heat and Mass Transfer*, 6th ed., John Wiley and Sons, Hoboken, NJ.

Bunker, R.S. and Metzger, D.E. (1990), "Local heat transfer in internally cooled turbine airfoil leading edge regions: part I – impingement cooling without film coolant extraction", *Journal of Turbomachinery*, Vol. 112 No. 3, pp. 451-458.

Calzada, P.D.L. and Alvarez, J.J. (2012), "Experimental investigation on the heat transfer of a leading edge impingement cooling system for low pressure turbine vanes", *Journal of Heat Transfer*, Vol. 132 No. 12, p. 122202.

Chupp, R.E., Helms, H.E. and Mcfadden, P.W. (1969), "Evaluation of internal heat transfer coefficients for impingement cooled turbine airfoils", *Journal of Aircraft*, Vol. 6 No. 3, pp. 203-208.

Cornaro, C., Fleischer, A.S. and Goldstein, R.J. (1999), "Flow visualization of a round jet impinging on cylindrical surfaces", *Experimental Thermal and Fluid Science*, Vol. 20 No. 2, pp. 66-78.

Délery, J.M. (2001), "Robert Legendre and Henri Werlé: toward the elucidation of three-dimensional separation", *Annual Review of Fluid Mechanics*, Vol. 33 No. 1, pp. 129-154.

Gbadebo, S.A., Cumpsty, N.A. and Hynes, T.P. (2005), "Three-dimensional separations in axial compressors", *Journal of Turbomachinery*, Vol. 127 No. 2, pp. 331-339.

Hirschel, E.H., Cousteix, J. and Kordulla, W. (2014), *Three-Dimensional Attached Viscous Flow*, Springer, Berlin, DE.

Jung, E.Y., Park, C.U., Lee, D.H., Kim, K.M. and Cho, H.H. (2018), "Effect of the injection angle on local heat transfer in a showerhead cooling with array impingement jets", *International Journal of Thermal Sciences*, Vol. 124, pp. 344-355.

Kan, X.X., Lu, H.W. and Zhong, J.J. (2016), "Topological characterization of vortex structures on a transonic compressor stator during the stalling process", *Proceedings of the Institution of Mechanical Engineers, Part G: Journal of Aerospace Engineering*, Vol. 230 No. 3, pp. 566-580.

Kumar, B.R. and Prasad, B.V.S.S.S. (2008), "Computational flow and heat transfer of a row of circular jets impinging on a concave surface", *Heat and Mass Transfer*, Vol. 44 No. 6, pp. 667-678.

Kwak, J.S. and Han, J.C. (2002), "Heat transfer coefficient and film-cooling effectiveness on a gas turbine blade tip", ASME Paper No. GT2002-30194.

Lee, C.H., Lim, K.B., Lee, S.H., Yoon, Y.J. and Sung, N.W. (2007), "A study of the heat transfer characteristics of turbulent round jet impinging on an inclined concave surface using liquid crystal transient method", *Experimental Thermal and Fluid Science*, Vol. 31 No. 6, pp. 559-565.

Legendre, R. (1956), "Séparation de l'écoulement laminaire tridimensionnel", *La Rech. Aéronaut*, Vol. 54, pp. 3-8.

Downloaded from ftp.nowpublishers.com/hff/article-pdf/31/12/3642/630499/hff-10-2020-0630.pdf by guest on 17 October 2026

Luo, L., Wang, C., Wang, S. and Sundén, B. (2016), "A numerical investigation of dimple effects on internal heat transfer enhancement of a double wall cooling structure with jet impingement", *International Journal of Numerical Methods for Heat and Fluid Flow*, Vol. 26 No. 7, pp. 2175-2197.

Luo, L., Zhang, Y., Wang, C., Wang, S. and Sundén, B.A. (2020), "On the heat transfer characteristics of a Lamilloy cooling structure with curvatures with different pin fins configurations", *International Journal of Numerical Methods for Heat and Fluid Flow*.

Menter, F.R. (1994), "Two-equation eddy-viscosity turbulence models for engineering applications", *AIAA Journal*, Vol. 32 No. 8, pp. 1598-1605.

Metzger, D.E. and Bunker, R.S. (1990), "Local heat transfer in internally cooled turbine airfoil leading edge regions: part II – impingement cooling with film coolant extraction", *Journal of Turbomachinery*, Vol. 112 No. 3, pp. 459-466.

Metzger, D.E., Yamashita, T. and Jenkins, C.W. (1969), "Impingement cooling of concave surfaces with lines of circular air jets", *Journal of Engineering for Power*, Vol. 91 No. 3, pp. 149-155.

Patil, V.S. and Vedula, R.P. (2018), "Local heat transfer for jet impingement onto a concave surface including injection nozzle length to diameter and curvature ratio effects", *Experimental Thermal and Fluid Science*, Vol. 92, pp. 375-389.

Poincaré, H. (1882), "Les points singuliers des équations différential", *C. R. Acad. Sci. Paris*, Vol. 94, pp. 416-418.

Qiu, D., Luo, L., Wang, S., Sundén, B.A. and Zhang, X. (2019), "Analysis of heat transfer and fluid flow of a slot jet impinging on a confined concave surface with various curvature and small jet to target spacing", *International Journal of Numerical Methods for Heat and Fluid Flow*, Vol. 29 No. 8, pp. 2885-2910.

Qiu, D., Wang, C., Luo, L., Wang, S., Zhao, Z. and Wang, Z. (2020), "On heat transfer and flow characteristics of jets impinging onto a concave surface with varying jet arrangements", *Journal of Thermal Analysis and Calorimetry*, Vol. 141 No. 1, pp. 57-68.

Rahman, M.M., Hernandez, C.F. and Lallave, J.C. (2010), "Free liquid jet impingement from a slot nozzle to a curved plate", *Numerical Heat Transfer, Part A: Applications*, Vol. 57 No. 11, pp. 799-821.

Taslim, M.E. and Khanicheh, A. (2006), "Experimental and numerical study of impingement on an airfoil leading edge with and without showerhead and gill film holes", *Journal of Turbomachinery*, Vol. 128 No. 2, pp. 310-320.

Taslim, M.E., Bakhtari, K. and Liu, H. (2003), "Experimental and numerical investigation of impingement on a rib-roughened leading-edge wall", ASME Paper No. GT2003-38118.

Versteeg, H.K. and Malalasekera, W. (2007), *An Introduction to Computational Fluid Dynamics: The Finite Volume Method*, 2nd ed., Pearson, London, UK.

Wallin, S. and Johansson, A.V. (2000), "An explicit algebraic Reynolds stress model for incompressible and compressible turbulent flows", *Journal of Fluid Mechanics*, Vol. 403, pp. 89-132.

Wang, N., Chen, A.F., Zhang, M. and Han, J.C. (2018), "Turbine blade leading edge cooling with one row of normal or tangential impinging jets", *Journal of Heat Transfer*, Vol. 140 No. 6, p. 062201.

Yang, G., Choi, M. and Lee, J.S. (1999), "An experimental study of slot jet impingement cooling on concave surface: effects of nozzle configuration and curvature", *International Journal of Heat and Mass Transfer*, Vol. 42 No. 12, pp. 2199-2209.

Yang, Y.T. and Hwang, C.H. (2004), "Numerical simulations on the hydrodynamics of a turbulent slot jet impinging on a semicylindrical convex surface", *Numerical Heat Transfer, Part A: Applications*, Vol. 46 No. 10, pp. 995-1008.

Downloaded from ftp.nowpublishers.com/hff/article-pdf/31/12/3642/630499/hff-10-2020-0630.pdf by guest on 17 October 2026

Yang, L., Ren, J., Jiang, H. and Ligrani, P. (2014), "Experimental and numerical investigation of unsteady impingement cooling within a blade leading edge passage", *International Journal of Heat and Mass Transfer*, Vol. 71, pp. 57-68.

Yang, L., Kan, R., Ren, J. and Jiang, H. (2013), "Effect of film cooling arrangement on impingement heat transfer on turbine blade leading edge", ASME Paper No. GT2013-95261.

Zhao, Z., Luo, L., Qiu, D., Wang, S., Wang, Z. and Sundén, B. (2020), "Vortical structures and heat transfer augmentation of a cooling channel in a gas turbine blade with various arrangements of tip bleed holes", *Numerical Heat Transfer, Part A: Applications*, pp. 1-28.

Further reading

ANSYS Fluent (2018), *Version 19.0*, ANSYS, Inc, Canonsburg, PA.

ANSYS ICEM CFD (2018), *Version 19.0*, ANSYS, Inc, Canonsburg, PA.

Corresponding author
Bengt Ake Sunden can be contacted at: bengt.sunden@energy.lth.se

For instructions on how to order reprints of this article, please visit our website:
www.emeraldgrouppublishing.com/licensing/reprints.htm
Or contact us for further details: **permissions@emeraldinsight.com**

Downloaded from ftp.nowpublishers.com/hff/article-pdf/31/12/3642/630499/hff-10-2020-0630.pdf by guest on 17 October 2026